RSC Advances

PAPER

View Article Online
View Journal | View Issue



Cite this: *RSC Adv.*, 2020, **10**, 35600

# Interaction of $LiYF_4:Yb^{3+}/Er^{3+}/Ho^{3+}/Tm^{3+}$@$LiYF_4:Yb^{3+}$ upconversion nanoparticles, molecularly imprinted polymers, and templates†

Hsiu-Wen Chien, *[a] Min-Ting Tsai,[b] Chien-Hsin Yang,[b] Rong-Ho Lee [c] and Tzong-Liu Wang *[b]

In this work, $LiYF_4:Yb_{0.25}^{3+}/Er_{0.01}^{3+}/Tm_{0.01}^{3+}/Ho_{0.01}^{3+}$@$LiYF_4:Yb_{0.2}^{3+}$ upconverting nanoparticles (UCNP) were used as luminescent materials for the preparation of molecular imprinting polymer nanocomposites. Three luminescent molecularly imprinted polymer (MIP) nanocomposites were prepared by *in situ* polymerization. The relationship between the functional monomers, templates, and upconversion nanoparticles was investigated. Two hydrophilic monomers (acrylic acid (AA) and acrylamide (AAm)) and one hydrophobic monomer (*N*-*tert*-butylacrylamide (TBAm)) were employed as functional monomers, while one amino acid (cysteine) and two proteins (albumin and hemoglobin) were employed as the templates to investigate the effect of their interaction with $LiYF_4:Yb^{3+}/Er^{3+}/Ho^{3+}/Tm^{3+}$@$LiYF_4:Yb^{3+}$ core/shell UCNPs on the polymerization process, luminescence properties, and adsorption capacity. The results showed that the UCNPs were embedded in the polymeric matrix to form an irregular quasimicrospherical UCNPs@MIP with diameters ranging from several hundred nanometers to several micrometers depending on the functional monomer. The quenching effect was more pronounced for the adsorption of hemoglobin with UCNPs@MIP compared to cysteine and albumin. In addition, the adsorption capacities of the AA- and AAm-made UCNPs@MIP were greater than those of TBAm-made UCNPs@MIP. The rebinding of the templates onto UCNPs@MIP was very fast and approached equilibrium within 30 min, indicating that the synthesized UCNPs@MIP can be employed as fluorescent probes to offer rapid detection of molecules.

Received 2nd July 2020
Accepted 21st September 2020

DOI: 10.1039/d0ra05771a

rsc.li/rsc-advances



## 1. Introduction

Molecular imprinting is a powerful method for the preparation of polymeric materials with tailor-made molecular recognition binding sites that have been used in applications such as chemical separations, catalysis, or molecular sensors.[1–3] The *in situ* polymerization of molecularly imprinted polymers (MIPs) is based on the copolymerization of the template and functional monomers through covalent/non-covalent interactions with crosslinkers.[4,5] After polymerization, these materials retain special cavities with corresponding steric and chemical memories upon the removal of the template. Therefore, the target species can selectively rebind to MIPs through specific interactions with these imprinted sites.[6]

Over recent decades, novel designed materials that couple MIPs with luminescent nanoparticles (NPs) have been explored as fluorescent probes to detect target molecules.[7–9] Among the luminescent NPs, rare earth element-doped upconversion NPs (UCNPs) are of great interest because of their high luminescence, lack of toxicity toward biological organisms, narrow absorption and emission peaks, long lifetime, and virtually zero interference background.[10,11] In addition, UCNPs can emit high-energy photons in the UV or visible regions of the electromagnetic spectrum under the excitation of low-energy near-infrared (NIR) photons. The use of NIR photons can also reduce autofluorescence so as to minimize the background light interference and improve the detection sensitivity.[12] Materials combining the advantages of UCNPs with MIPs are promising labels.

Even though some of the nanocomposites of MIP with UCNPs have been used as a fluorescence determination platform,[13–17] very few investigations focusing on understanding the polymer–template–UCNPs interactions and their relationship to material performance have been carried out. Therefore, this work focuses on the study of the interaction between the

[a]*Department of Chemical and Materials Engineering, National Kaohsiung University of Science and Technology, Kaohsiung 807, Taiwan. E-mail: hsiu-wen.chien@nkust.edu.tw; Fax: +886-7-3830674*

[b]*Department of Chemical and Materials Engineering, National University of Kaohsiung, Kaohsiung 811, Taiwan. E-mail: tlwang@nuk.edu.tw; Fax: +886-7-591-9368 ext. 5000*

[c]*Department of Chemical Engineering, National Chung Hsing University, Taichung 402, Taiwan*

† Electronic supplementary information (ESI) available. See DOI: 10.1039/d0ra05771a

different functional monomers, templates, and UCNPs to provide guidance for the design of nanocomposites of UCNPs with MIPs (UCNPs@MIP). Our recent study reported the synthesis of tri-doped $LiYF_4$:$Yb^{3+}$/$Er^{3+}$/$Ho^{3+}$/$Tm^{3+}$@$LiYF_4$:$Yb^{3+}$ core/shell UCNPs with two strongest emission peaks at approximately 540 nm and 650 nm upon NIR excitation.[18] We combined tri-doped UCNPs with three template molecules, namely cysteine (Cys), albumin (Alb), and hemoglobin (Hb), and three functional monomers, namely acrylic acid (AA), acrylamide (AAm), and *N-tert*-butyl acrylamide (TBAm), to synthesize nine UCNPs@MIP nanocomposites *via in situ* polymerization (Fig. 1). Transmission electron microscopy (TEM), Fourier-transform infrared spectroscopy (FTIR), ultraviolet-visible spectroscopy (UV-vis), and photoluminescence (PL) were used to characterize the UCNPs@MIP nanocomposites to understand the interaction between the UCNPs, functional monomers, and templates.

## 2. Experimental section

### 2.1. Synthesis of UCNPs

Nanoparticles of $LiYF_4$ doped with $Yb^{3+}$, $Er^{3+}$, $Ho^{3+}$, and $Tm^{3+}$ ions were synthesized by the thermal decomposition of the lanthanide and lithium trifluoroacetate precursors in the presence of oleic acid coordinating ligands and noncoordinating 1-octadecene solvent molecules, according to our previously reported procedure.[18–20] Briefly, a batch of $Yb^{3+}$-, $Er^{3+}$-, $Ho^{3+}$-, and $Tm^{3+}$-doped $LiYF_4$ (74 mol% Y, 20 mol% Yb, 2 mol% Er, 2 mol% Ho, and 2 mol% Tm) was obtained as follows: $Li_2CO_3$ (1.48 mmol), $Y_2O_3$ (0.74 mmol), $Yb_2O_3$ (0.2 mmol), $Er_2O_3$ (0.02 mmol), $Ho_2O_3$ (0.02 mmol), and $Tm_2O_3$ (0.02 mmol) were dissolved in 50% trifluoroacetic acid (TFA) at 80 °C in a three-necked flask. Then, the solutions were evaporated to dryness under an argon gas purge. Next, oleic acid (15 mL) and 1-octadecene (15 mL) were added to the three-necked flask. The resulting solution was then heated to 120 °C at a rate of approximately 2 °C $min^{-1}$ with magnetic stirring for 30 min to remove water and oxygen. The light-yellow solution was then heated to 300 °C at a rate of approximately 30 °C per minute under argon gas protection, and kept at 300 °C under vigorous stirring for approximately 1 h. The mixture was cooled to room temperature and precipitated with ethanol. The solid was collected by centrifugation at 8000 rpm for 10 min, and then dispersed and re-precipitated from ethanol two times to obtain the oleate-capped $LiYF_4$:$Yb_{0.25}^{3+}$/$Ho_{0.01}^{3+}$/$Tm_{0.01}^{3+}$/$Er_{0.01}^{3+}$ core nanoparticles.

For shell growth, $Li_2CO_3$ (1.6 mmol), $Y_2O_3$ (0.8 mmol), and $Yb_2O_3$ (0.2 mmol) were dissolved in 50% TFA at 80 °C in a three-necked flask. Next, oleic acid (15 mL) and 1-octadecene (15 mL) were added to the three-necked flask under vacuum. The resulting solution was heated to 120 °C at a rate of approximately 2 °C $min^{-1}$ for 30 min and then $LiYF_4$:$Yb_{0.25}^{3+}$/$Ho_{0.01}^{3+}$/$Tm_{0.01}^{3+}$/$Er_{0.01}^{3+}$ cores were added under vigorous stirring to remove water and cyclohexane. The light-yellow solution was then heated to 300 °C at a rate of approximately 30 °C per minute under argon gas protection for 1 h. The mixture was cooled to room temperature and precipitated with ethanol. The solid was collected by centrifugation at 8000 rpm for 10 min, and then dispersed and re-precipitated from ethanol twice to obtain the oleate-capped $LiYF_4$:$Yb_{0.25}^{3+}$/$Ho_{0.01}^{3+}$/$Tm_{0.01}^{3+}$/$Er_{0.01}^{3+}$@$LiYF_4$:$Yb_{0.20}^{3+}$ core/shell nanoparticles.

### 2.2 Preparation of UCNPs@MIPs

The molecularly imprinted polymer nanocomposites were prepared *via* an *in situ* polymerization method. Three monomers were used for polymerization, namely acrylic acid (AA), acrylamide (AAm), and *N-tert*-butyl acrylamide (TBAm), while

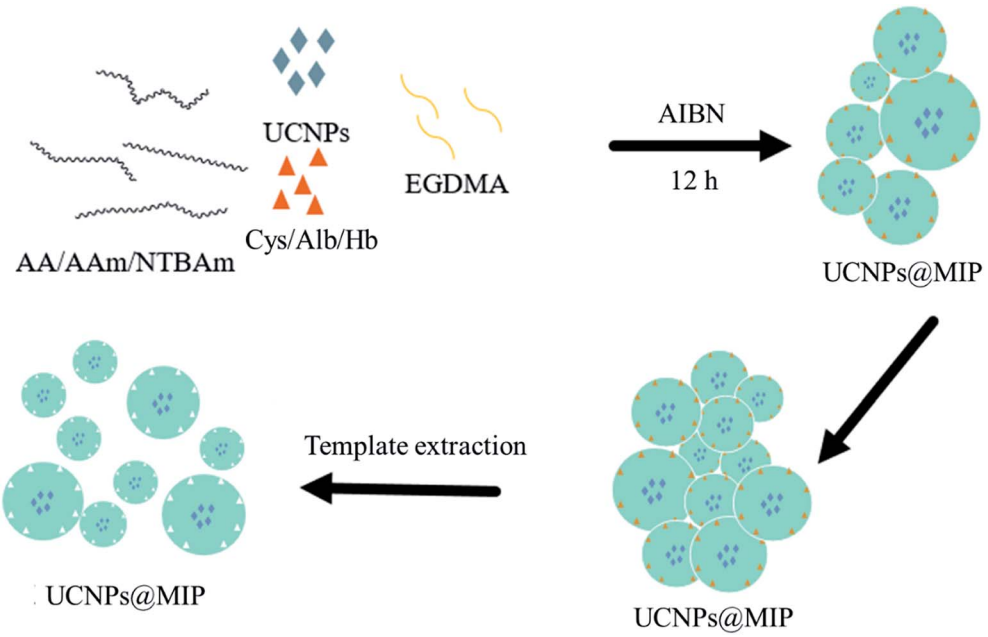


Fig. 1 Schematic representation of the preparation processes for the UCNPs@MIP.

cysteine (Cys), albumin (Alb), and hemoglobin (Hb) were used as the template molecules. The template molecules were first dissolved in ethanol (100 mL) in a three-necked round-bottom flask under argon protection, followed by the addition of azobisisobutyronitrile (AIBN) (0.1 g), functional monomers (1 mole), ethylene glycol dimethylacrylate (EGDMA) (1 mol), and $LiYF_4$:$Yb_{0.25}^{3+}$/$Ho_{0.01}^{3+}$/$Tm_{0.01}^{3+}$/$Er_{0.01}^{3+}$@$LiYF_4$:$Yb_{0.20}^{3+}$ core/shell nanoparticles (1 g). The reaction mixture was maintained at 60 °C for 48 h. After polymerization, the composites were collected by filtration and washed several times with methanol and water to remove the unreacted monomers and other ingredients. The dried nanocomposites were further pulverized using an agate mortar (UCNPs@MIP). For the control experiment, the non-imprinted polymer nanocomposites were synthesized by applying the same procedure without the template molecules, and the obtained sample was called UCNPs@NIP.

To remove the template molecules from the imprinted nanocomposites, the imprinted nanocomposites were dipped into the acetic acid/ethanol (1/9, v/v) solution repeatedly to break the interactions between the template molecules and the functional monomer. After the final washing step, the MIP nanocomposites were dispersed in ethanol and stored at 4 °C.

### 2.3. Characterization of UCNPs and UCNPs@MIP

Wide-angle X-ray diffractograms (WAXD) were obtained with a Bruker D8 ADVANCE diffractometer, using Cu Ka radiation with a step size of 0.05° and a scanning speed of 4° $min^{-1}$. Transmission electron microscopy (TEM) images were obtained using a JEOL JEM1230 transmission electron microscope. Dynamic light scattering (DLS) measurements were achieved by a Brookhaven Instruments 90PLUS instrument. Fourier-transform infrared spectroscopy (FTIR) spectra were recorded using a Spectrum GX FTIR spectrometer (PerkinElmer, Inc.). The transmission spectra of the KBr sample pellets were collected with a resolution of 4 $cm^{-1}$, acquiring a total of 16 scans in a wavenumber region of 400–4000 $cm^{-1}$. Ultraviolet-visible (UV-vis) spectroscopic analysis was performed using a PerkinElmer Lambda 35 UV-vis spectrophotometer. Photoluminescence (PL) spectra were recorded on a Hitachi F-7000 fluorescence spectrophotometer (Japan). The emission spectra of the nanocrystals were obtained upon 980 nm NIR excitation using a SDL980-LM-5000T laser diode (980 nm, 3 W $cm^{-2}$) obtained from Shanghai Dream Lasers Technology Co., Ltd. (China).

### 2.4 Binding experiments

For the kinetic adsorption experiments, UCNPs@MIP (50 mg) and either Cys, or Alb, or Hb solution (100 mL) with a concentration of 0.5 mg $mL^{-1}$ were mixed in a tube. The mixed solution was shaken for different times (0, 15, 30, 45, 60, and 75 min) at room temperature. After rebinding of the templates and UCNPs@MIP, the mixture was centrifuged at 10 000 rpm for 10 min, and the supernatant was collected and analyzed using a UV-vis spectrophotometer. The concentration of each sample was calculated based on the standard curve. The UCNPs@NIP was also treated in the same manner for comparison. The adsorption capacity ($Q$) was calculated using the mass balance equation:[21,22]

$$Q(\text{mg g}^{-1}) = \frac{(C_i - C_r)V}{m}$$

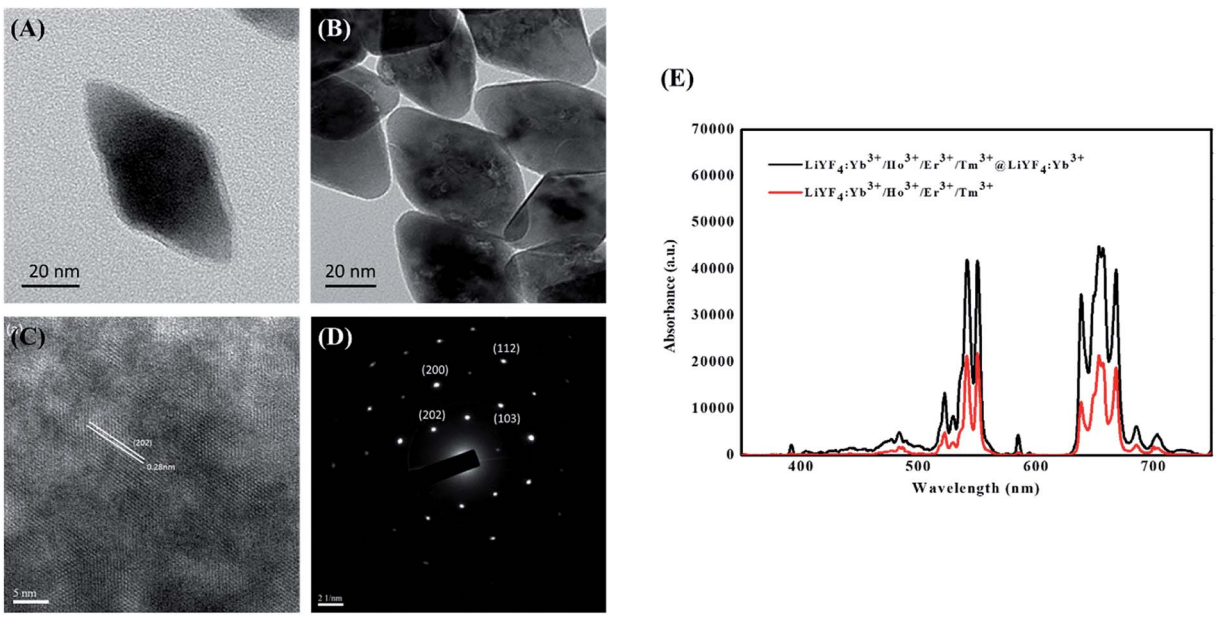


Fig. 2 TEM images of the $LiYF_4$:$Yb_{0.25}^{3+}$/$Ho_{0.01}^{3+}$/$Tm_{0.01}^{3+}$/$Er_{0.01}^{3+}$ core (A) and $LiYF_4$:$Yb_{0.25}^{3+}$/$Ho_{0.01}^{3+}$/$Tm_{0.01}^{3+}$/$Er_{0.01}^{3+}$@$LiYF_4$:$Yb_{0.20}^{3+}$ core/shell (B) nanoparticles. High-resolution TEM image of the single-crystalline structure (C) and the SAED pattern (D) of $LiYF_4$:$Yb_{0.25}^{3+}$/$Ho_{0.01}^{3+}$/$Tm_{0.01}^{3+}$/$Er_{0.01}^{3+}$@$LiYF_4$:$Yb_{0.20}^{3+}$ core/shell (×300 K). (E) Photoluminescence spectra of tri-doped $LiYF_4$:$Yb_{0.25}^{3+}$/$Ho_{0.01}^{3+}$/$Tm_{0.01}^{3+}$/$Er_{0.01}^{3+}$ core and $LiYF_4$:$Yb_{0.25}^{3+}$/$Ho_{0.01}^{3+}$/$Tm_{0.01}^{3+}$/$Er_{0.01}^{3+}$@$LiYF_4$:$Yb_{0.20}^{3+}$ core/shell under 980 nm excitation light.

 

where $C_i$ (mg mL$^{-1}$) is the initial concentration of the template in the aqueous solution, $C_r$ (mg mL$^{-1}$) is the concentration of the template in the supernatant solution after adsorption, $m$ (mg) is the mass of adsorbent, and $V$ (mL) is the volume of the solution.

## 3. Results and discussion

### 3.1. Characterization of the upconverting nanoparticles

First, the structure, morphology, and optical properties of the $LiYF_4$:$Yb_{0.25}^{3+}$/$Ho_{0.01}^{3+}$/$Tm_{0.01}^{3+}$/$Er_{0.01}^{3+}$@$LiYF_4$:$Yb_{0.20}^{3+}$ nanoparticles were investigated. The phase structures of the nanoparticles were investigated by wide-angle X-ray diffraction (WAXD). The peaks observed in the XRD diffraction patterns at the $2\theta$ of 18, 29, 31, 33, 34, 40, 42, 46, 47, 49, 50, 54, 58, 59, 62, 63, and 66 degrees were attributed to the (101), (112), (103), (004), (200), (202), (211), (114), (105), (123), (204), (220), (301), (116), (132), (224), and (206) planes of the tetragonal $LiYF_4$ crystal. The WAXD results indicate that the relative intensity and position of all of the diffraction peaks closely match the Joint Committee on Powder Diffraction Standards (JCPDS) file no. 17e0874. After coating the $LiYF_4$:$Yb^{3+}$ shell, the XRD patterns of the core/shell nanoparticles showed peaks similar to those of the core nanoparticles, as shown in Fig. S1.† The similar patterns of the $LiYF_4$:$Yb_{0.25}^{3+}$/$Ho_{0.01}^{3+}$/$Tm_{0.01}^{3+}$/$Er_{0.01}^{3+}$ core and $LiYF_4$:$Yb_{0.25}^{3+}$/

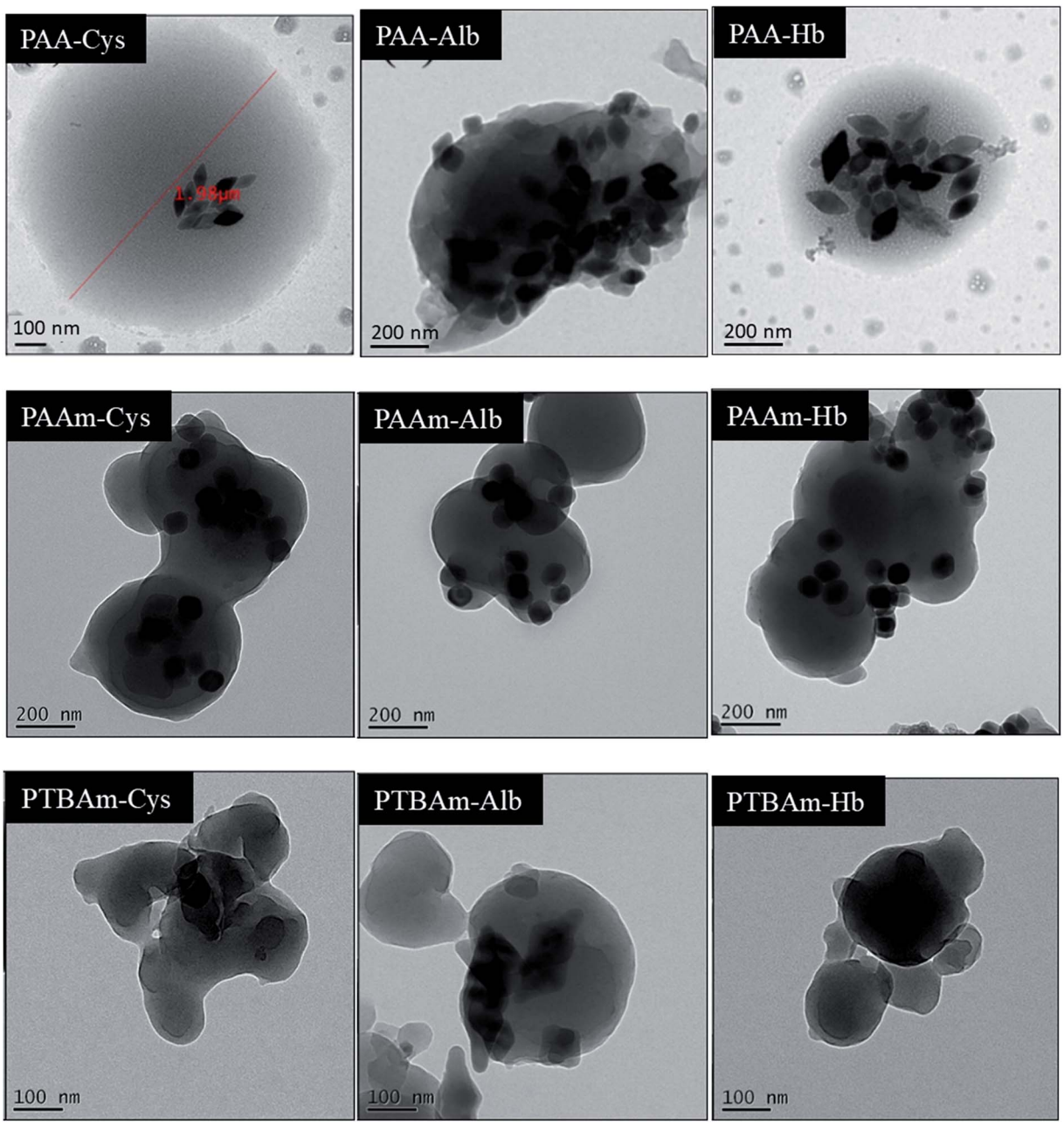


Fig. 3 TEM images of UCNPs@MPS of PAA, PAAm, and PTBAm with cysteine, albumin, and hemoglobin binding.

$Ho_{0.01}^{3+}/Tm_{0.01}^{3+}/Er_{0.01}^{3+}$@$LiYF_4$:$Yb_{0.20}^{3+}$ core/shell nanoparticles can be attributed to the extremely low shell thickness.

The particle shapes and crystal structures of the synthesized nanoparticles were investigated by TEM. As observed from the images presented in Fig. 2A and B, the core and core/shell nanoparticles are tetragonal nanoparticles with octahedral morphology. The average dimensions of the core nanoparticles obtained from TEM image analysis were approximately 78 nm along the long axis and 40 nm along the short axis. After coating the $LiYF_4$:$Yb^{3+}/Er^{3+}/Tm^{3+}/Ho^{3+}$ cores with the $LiYF_4$:$Yb^{3+}$ shell, the short axis lengths of the tetragonal crystals for the core/shell nanoparticles increased significantly to 44.3 ± 1.2 nm. The HRTEM images exhibit well-resolved *d*-spacings of $LiYF_4$:$Yb_{0.25}^{3+}/Ho_{0.01}^{3+}/Tm_{0.01}^{3+}/Er_{0.01}^{3+}$@$LiYF_4$:$Yb_{0.20}^{3+}$ core/shell nanoparticles that match well with the distance between the (202) planes in the $LiYF_4$ of the single-crystalline structure (Fig. 2C). The selected area electron diffraction (SAED) patterns presented in Fig. 2D show that the patterns consist of many spots indexed to the corresponding (*hkl*) planes according to the standard JCPDS no. 17e0874. The SAED patterns further demonstrate that the formed $LiYF_4$:$Yb_{0.25}^{3+}/Ho_{0.01}^{3+}/Tm_{0.01}^{3+}/Er_{0.01}^{3+}$@$LiYF_4$:$Yb_{0.20}^{3+}$ core/shell nanoparticles have a single-crystal tetragonal phase structure.

Fig. 2E shows the emission spectra of the $LiYF_4$:$Yb_{0.25}^{3+}/Ho_{0.01}^{3+}/Tm_{0.01}^{3+}/Er_{0.01}^{3+}$ cores and $LiYF_4$:$Yb_{0.25}^{3+}/Ho_{0.01}^{3+}/Tm_{0.01}^{3+}/Er_{0.01}^{3+}$@$LiYF_4$:$Yb_{0.20}^{3+}$ core/shell nanoparticles upon 980 nm excitation. When the core and core/shell nanoparticles are excited with the 980 nm laser, $Yb^{3+}$ first absorbs the energy of the 980 nm irradiation and then excites $Er^{3+}$, $Ho^{3+}$, and $Tm^{3+}$, leading to electronic transitions. Therefore, we observed two emission bands at approximately 540 nm and 650 nm that resulted from the $Yb^{3+}$ to $Er^{3+}$ transitions of $^2H_{11/2} \rightarrow {}^4I_{15/2}$ (525

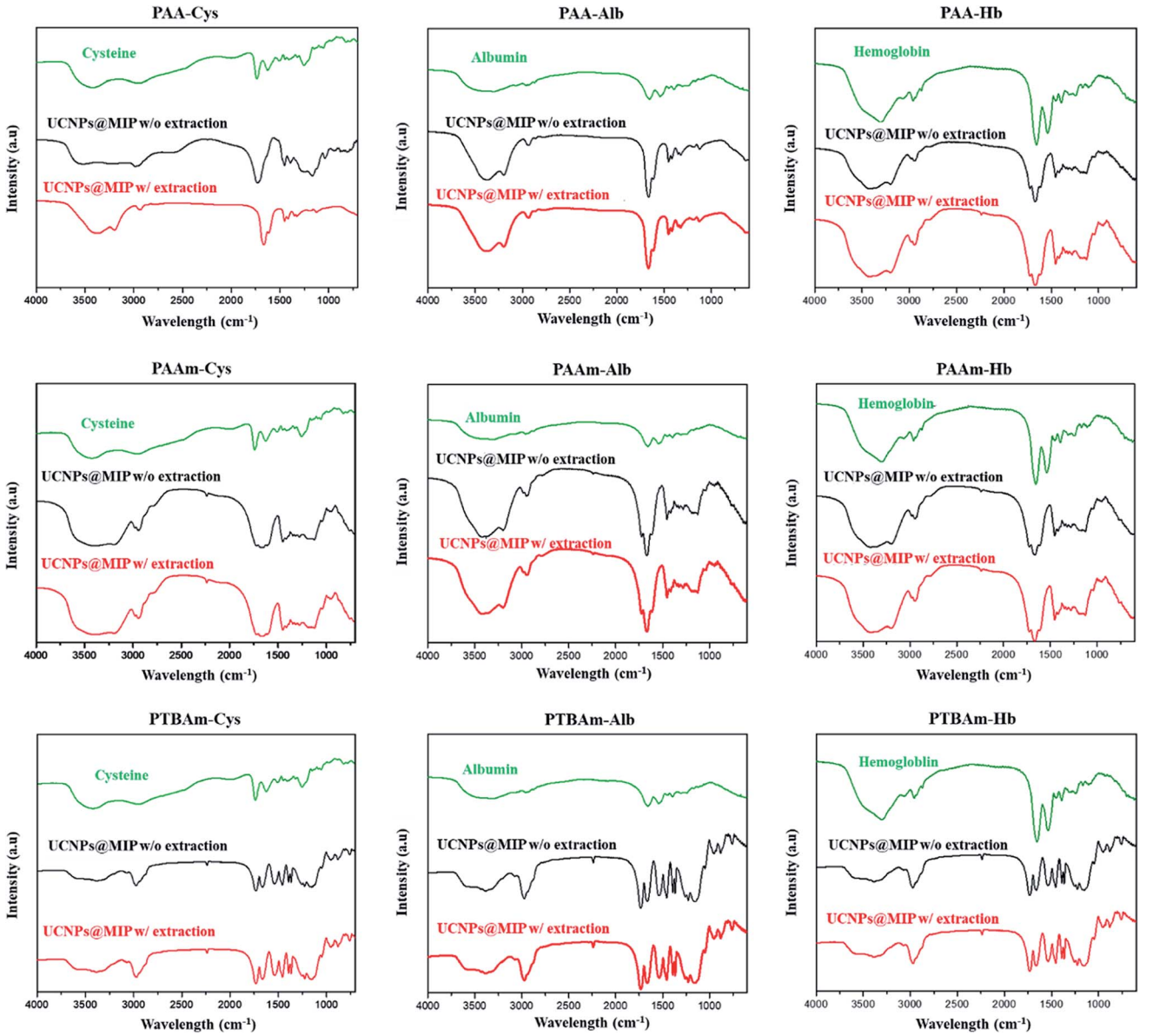


Fig. 4 FTIR spectra of templates of cysteine, albumin, and hemoglobin in UCNPs@MIP with (w/) and without (w/o) template extraction.

 

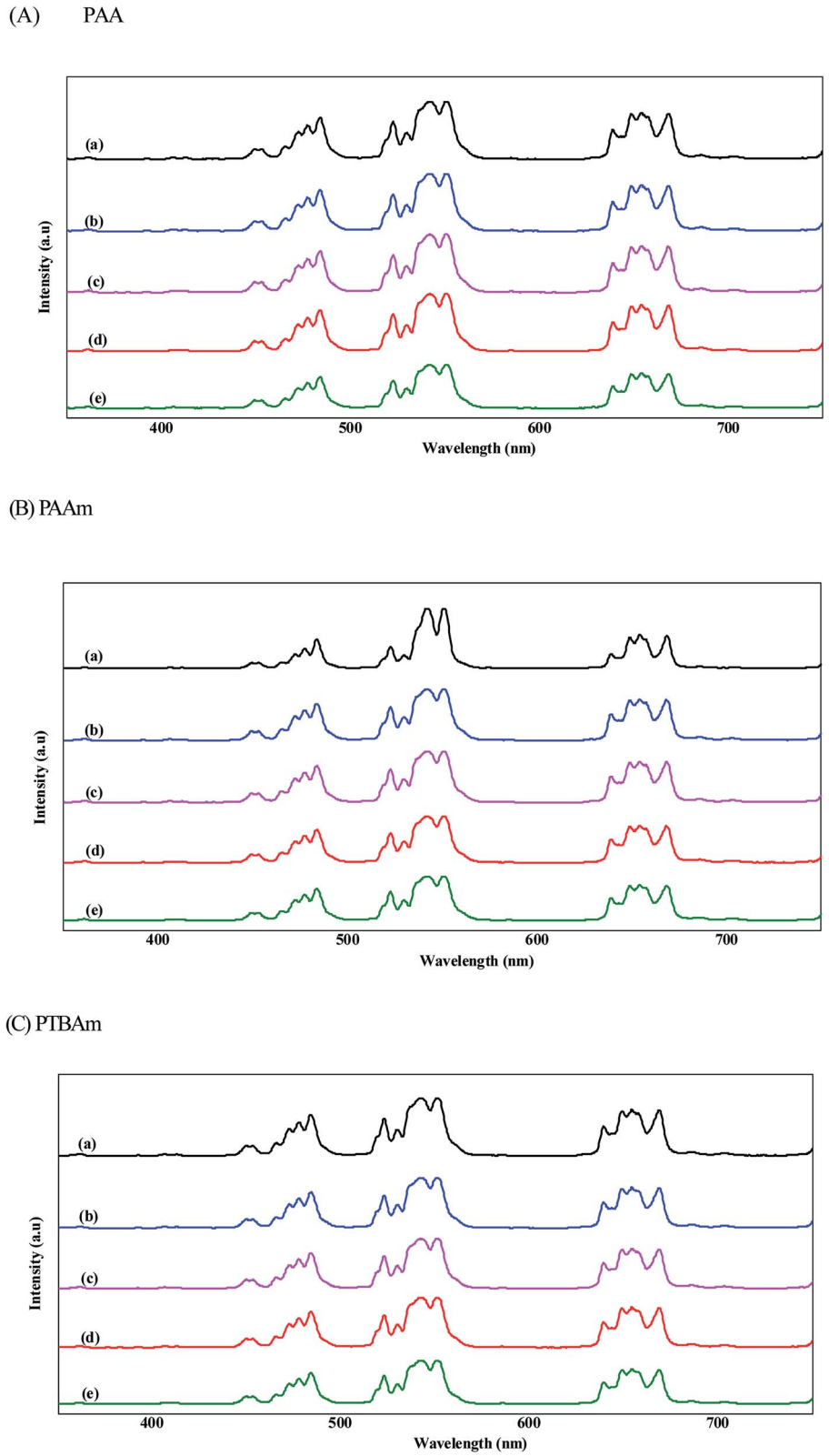


Fig. 5 Photoluminescence spectra of UCNPs@MIP of PAA (A), PAAm (B), and PTBAm (C) with template binding. (a) UCNPs; (b) UCNPs@NIP; UCNPs@NIP with (c) cysteine; (d) albumin; and (e) hemoglobin binding.

nm), $^4S_{3/2} \rightarrow {}^4I_{15/2}$ (540 nm), and $^4F_{9/2} \rightarrow {}^4I_{15/2}$ (660 nm), the $Yb^{3+}$ to $Ho^{3+}$ transitions of $^5F_4 \rightarrow {}^5I_8$ (541 nm) and $^5F_5 \rightarrow {}^5I_8$ (650 nm), and the $Yb^{3+}$ to $Tm^{3+}$ transitions of $^1D_2 \rightarrow {}^3F_4$ (450 nm), $^1G_4 \rightarrow {}^3H_6$ (475 nm), and $^1G_4 \rightarrow {}^3F_4$ (650 nm).[18] After coating with the $LiYF_4$:$Yb^{3+}$ shell, it is apparent that the emissions in the core/shell nanoparticles were stronger than the

corresponding emissions in the core nanoparticles. In the energy transfer process, the photoexcited dopants located on or near the surface can be deactivated directly by neighboring quenching centers.[23,24] Moreover, the energy contained in the photoexcited dopants located in the center of nanophosphors can randomly migrate and travel a long distance to the dopant on or near the surface or directly to the surface quenching sites.[25,26] Here, we utilized the active core/active shell structure that can avoid energy quenching to achieve a high upconversion photoluminescence efficiency.

### 3.2 Characterization of UCNPs@MIP

All UCNPs@MIP composites were prepared by copolymerization of functional monomers (AA, AAm, or TBAm) and EGDMA in the presence of $LiYF_4$:$Yb_{0.25}^{3+}$/$Ho_{0.01}^{3+}$/$Tm_{0.01}^{3+}$/$Er_{0.01}^{3+}$@-$LiYF_4$:$Yb_{0.20}^{3+}$ core/shell nanoparticles and templates (Cys, Alb, or Hb). The morphology of the prepared UCNPs@MIP was observed by TEM (Fig. 3). We observed that many UCNPs were embedded in the polymeric matrix to form an irregular quasi-microsphere, indicating that the UCNPs are incorporated into the polymer matrix during the polymerization process. The irregular quasimicrospherical structures have various configurations depending on the functional monomers used. Using AA, AAm, and TBAm as the functional monomers, the average sizes of the obtained spheres determined TEM were approximately 1001 ± 130, 475 ± 54, and 305 ± 75 nm, respectively. On the other hand, the size (hydrodynamic diameter) of AA-, AAm-, and TBAm-made UCNPs@MIP by dynamic light scattering (DSL) was about 2084, 1396, and 435 nm, respectively (Fig. S2†). The values by DSL (wet type analysis) were nearly 1.5–3 fold higher than those by TEM (dry type analysis), respectively, which indicates swelling of the polymers in water. The irregularity of the morphologies is presumed to be due to the presence of two simultaneous polymerization mechanisms, with a phase inversion polymerization producing larger microspheres and precipitation polymerization giving rise to the smaller microspheres.[27]

The embedding of UCNPs into the polymeric matrix was further confirmed by FTIR spectroscopy. The FTIR spectra of free templates, and UCNPs@MIP with and without template extraction were recorded in the range of 400–4000 $cm^{-1}$ (Fig. 4). For an example of UCNPs@MIPs with BSA embedding, the absorption peaks of free Alb are the protein amide I band at 1655 $cm^{-1}$ (mainly C=O stretch) and amide II band at 1535 $cm^{-1}$ (C–N stretching coupled with N–H bending modes). For the Alb embedded into the UCNPs@MIPs that were obtained from AA and EGDMA, the typical peaks at 3400 $cm^{-1}$ (O–H stretching) and 1687 $cm^{-1}$ (C=O stretching in –COOH) indicated that PAA was successfully formed, while the peak at 1625 $cm^{-1}$ corresponds to the stretching vibrations of C=O of EGDMA, indicating that the EGDMA crosslinkers were successfully incorporated into the imprinted polymers. It is important to note that the signals of Alb were hardly observed in the UCNPs@MIP material without template extraction, most likely due to the low amount of Alb incorporated in the polymer network. In addition, the major bands of UCNPs@MIP with and

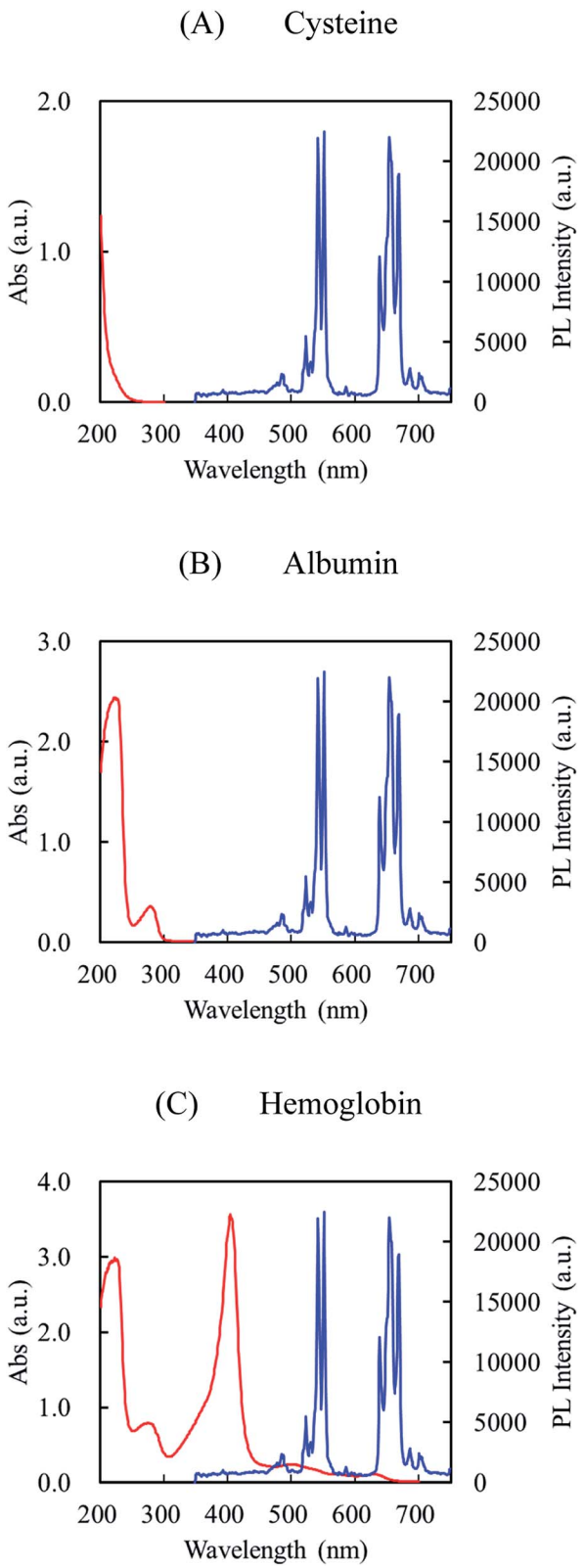


Fig. 6 UV-vis absorption spectra (red color) of cysteine (A), albumin (B), and hemoglobin (C) and fluorescence emission spectrum (blue color) of UCNPs.

without template extraction appeared in similar locations. These results suggested that UCNPs@MIP was successfully synthesized and was highly stable.

The PL spectra of the initial UCNPs, UCNPs@NIP, and UCNP@MIP with three templates are shown in Fig. 5. First, we discuss the fluorescence intensity of the UCNPs and AA-, AAm-, and TBAm-made UCNPs@NIP, respectively. The results showed that the fluorescence intensity decreased only slightly after coating with NIP, indicating that the polymer coating did not influence the luminescent properties of UCNPs. Next, we discuss the fluorescence intensity of the UCNPs@MIP with Cys, Alb, and Hb binding. It is observed that the fluorescence intensity slightly decreased after the UCNPs@MIP bond with Cys and Alb (about 12% fluorescence quenching at 550 nm). However, the fluorescence intensity was significantly quenched when Hb was bound to the UCNPs@MIP (more than 25% fluorescence quenching at 550 nm). The quenching phenomenon can generally be explained as follows: the first is the energy transfer, which contributing from the spectral overlap between the absorption spectrum of the template and the emission spectrum of the UCNPs@MIP;[28,29] and the second is the charge transfer, which contributing from the interaction between UCNPs, templates, and MIPs through electrostatic interaction or hydrogen bond.[13,30] When the existence of templates, the electrons at the conductive band of the UCNPs@MIP could transfer to the lowest unoccupied molecular orbital of templates.[30,31] For Cys and Alb, they had adsorption bands at 200 and 280 nm, respectively, which were far away from the emission spectrum of UCNPs@MIP (Fig. 6A and B). Thus, we considered that the fluorescence quenching behavior would be attributed to the charge transfer between templates (Cys and Alb) and UCNPs@MIPs. For Hb, the UV-vis absorption of Hb was at around 280, 400, and 508 nm, which was near to the emission spectrum of UCNPs@MIP (Fig. 6C). In addition, the spectral overlap at a wavelength of 500 nm between the absorption spectrum of Hb and the emission spectrum of the UCNPs@MIP. We speculate that the quenching effect is probably caused by the simultaneous occurrence of energy transfer

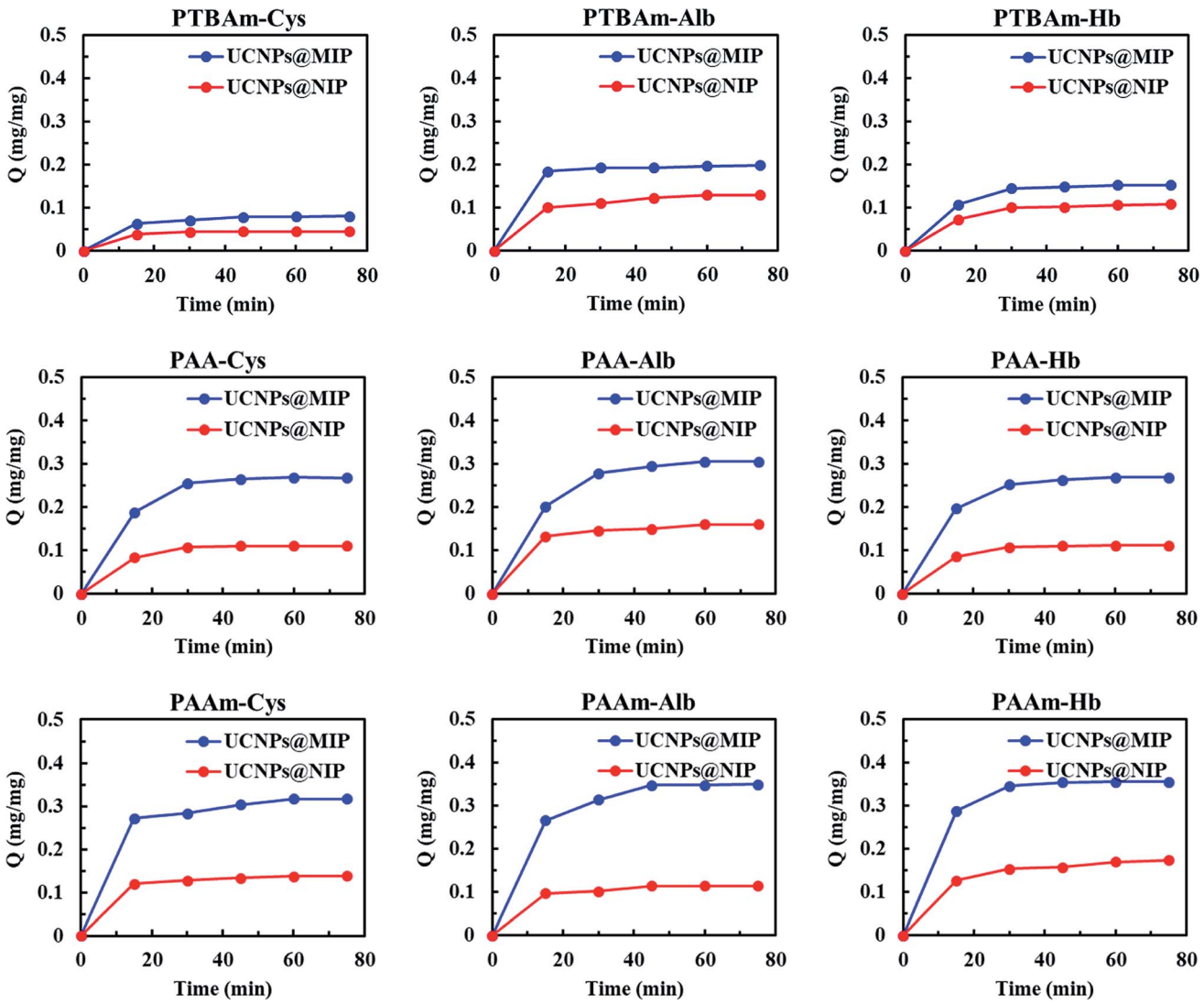


Fig. 7 Adsorption kinetics of cysteine, albumin, and hemoglobin in PAA, PAAm, and PTBAm UCNPs@MIP and UCNPs@NIP.

and charge transfer. Thus, the fluorescence intensity obviously decreased when Hb was bound to the UCNPs@MIP.

### 3.3 Equilibrium binding

The kinetic adsorption process of UCNPs@MIP and UCNPs@-NIP (AA-, AAm-, and TBAm-made) was conducted by incubating either UCNPs@MIP (50 mg) or UCNPs@NIP (50 mg) at a fixed concentration of Cys, Alb, or Hb solution for different time periods. As shown in Fig. 7, the results suggest that AA- and AAm-made UCNPs@MIPs showed a high adsorption rate in the first 15 min, and the adsorption capacity was close to saturation after 30 min, while TBAm-made UCNPs@MIP almost reached equilibrium after 15 min of incubation. In addition, the three AA-, AAm-, and TBAm-made UCNPs@NIPs reached adsorption equilibrium within 15 min. Overall, the adsorption capacity of the UCNPs@MIPs was much larger than that of UCNPs@NIPs under the same template. For example, in Cys adsorption in AA-made nanocomposites, there were 0.255 and 0.107 mg $mg^{-1}$ binding UCNP@MIP and UCNPs@NIP within 30 min, respectively. The much higher adsorption is due to the imprinted UCNPs@MIPs exhibiting a high specific binding ability for the templates compared to the non-imprinted UCNPs@NIPs. The results showed excellent evidence for the efficient imprinting effect of UCNPs@MIPs. In addition, the equilibrium time of the UCNPs@MIPs in this work was also shorter than that of the other imprinting systems.[32,33] This demonstrates that the resulting UCNPs@MIPs have good mass transport properties for rebinding of the templates.

Generally, the imprinting efficiency depends strongly on many factors such as the strength of the interactions between the template and the functional monomer, that is, different functional monomers lead to dissimilar performance of MIPs. For our results, it is important to note that the adsorption capacity values of Cys in the AA-, AAm-, and TBAm-made UCNPs@MIP were 0.255, 0.284, and 0.071 mg $mg^{-1}$ within 30 min, respectively. Similar trends were also found for the Alb and Hb adsorption in the AA-, AAm-, and TBAm-made UCNPs@MIP. These results suggested that the adsorption capacity of the hydrophilic monomer-made UCNPs@MIP is greater than that of the hydrophobic monomer-made UCNPs@MIP. Generally, hydrophobic residues of most proteins are sequestered in the core of the native structure, while polar residues are present on the surface.[34] A polymer matrix that offers hydrophilic functional groups easily forms hydrogen bond acceptor or donor groups within a suitable region on the surface of a protein. In contrast to the hydrophilic monomer, TBAm belongs to the class of hydrophobic functional monomers, and is regarded as a $\pi$–$\pi$ donor,[35] and therefore, it has difficulty in binding with polar residues, limiting the adsorption process. Thus, the use of an aqueous medium can provide a favorable environment for proteins in the protein imprinting process. In addition, AA generally shows electrostatic interaction with the template at neutral conditions, while AAm can provide multiple hydrogen binding sites with templates.[36] The results showed that the adsorption capacity of the AAm-made UCNPs@MIP was improved related to that of the AA-made UCNPs@MIP. We speculated that amide groups can form stronger hydrogen bonds with the template molecules than the carboxyl groups of AA. Therefore, AAm-made UCNPs@MIP showed the highest overall binding capacity.

Despite the many advantages of MIPs, the preparation of a novel MIP has many challenges based on different substrates. Thus, different combinations of monomers and crosslinkers are required to adequately form the imprinted polymers for that substrate. Previous studies reported that the introduction of charged monomers into the polymer network can promote stronger template–imprint interactions through electrostatic interactions.[37] However, charged residues can also cause non-specific binding of the template, resulting in a reduced imprinting effect.[37] In addition, the crosslinking process can ensure the preservation of the imprint cavity after removal of the template. The imprinted cavities may collapse easily if there is a low degree of crosslinking, while an excessive crosslinking density may restrict templates mobility within polymer networks, leading to slower template removal, or permanent entrapment of the template in the polymer network, leading to poor rebinding efficiency.[38] Moreover, the grafting of MIPs shells onto UCNPs cores is easy to form aggregation, resulting in poor penetration of light through the dense suspension.[39] Our study demonstrated that the synthesized UCNPs can incorporated with MIPs be employed as fluorescence probes for the rapid detection of molecules. However, the sensitivity and selectivity need further verify. In order to design effective cavities with excellent spatial matching effect, more functional monomers will be worth exploring to in the future.

## 4. Conclusions

In this study, we synthesized nine UCNPs@MIP nanocomposites to study the interaction between the three functional monomers (AA, AAm, and TBAm), three templates (Cys, Alb, and Hb), and UCNPs. TEM images show that the morphology of nine UCNPs@MIP is irregular quasimicrospherical due to phase inversion polymerization and precipitation polymerization. In the PL experiments, fluorescence quenching occurred obviously in Hb bound to UCNPs@MIP compared to in Cys and Alb because of accompanied effects of charge transfer and energy transfer. Dynamic rebinding tests showed that the adsorption capacities of the AA- and AAm-made UCNPs@MIP were greater than those of TBAm-made UCNPs@MIP because hydrophilic AA and AAm offer electrostatic interactions and hydrogen binding sites, respectively, to bind the templates. Overall, our results demonstrate that the synthesized UCNPs@MIP can be employed as a fluorescence probe for rapid detection.

## Conflicts of interest

The authors declare that there are no conflicts of interest.

## Acknowledgements

We gratefully acknowledge the support of the Ministry of Science and Technology in Taiwan through Grant MOST 107-2221-E-390-004.

 

## References

1 R. A. S. Alatawi, M. Monier and N. H. Elsayed, Chiral separation of (+/−)-methamphetamine racemate using molecularly imprinted sulfonic acid functionalized resin, *J. Colloid Interface Sci.*, 2018, **531**, 654–663.
2 M. Resmini, Molecularly imprinted polymers as biomimetic catalysts, *Anal. Bioanal. Chem.*, 2012, **402**, 3021–3026.
3 S. Piletsky, F. Canfarotta, A. Poma, A. M. Bossi and S. Piletsky, Molecularly imprinted polymers for cell recognition, *Trends Biotechnol.*, 2020, **38**, 368–387.
4 K. Karim, F. Breton, R. Rouillon, E. V. Piletska, A. Guerreiro, I. Chianella and S. A. Piletsky, How to find effective functional monomers for effective molecularly imprinted polymers?, *Adv. Drug Delivery Rev.*, 2005, **57**, 1795–1808.
5 S. Beyazit, B. Tse Sum Bui, K. Haupt and C. Gonzato, Molecularly imprinted polymer nanomaterials and nanocomposites by controlled/living radical polymerization, *Prog. Polym. Sci.*, 2016, **62**, 1–21.
6 L. Chen, X. Wang, W. Lu, X. Wu and J. Li, Molecular imprinting: perspectives and applications, *Chem. Soc. Rev.*, 2016, **45**, 2137–2211.
7 Y. Ma, S. Xu, S. Wang and L. Wang, Luminescent molecularly-imprinted polymer nanocomposites for sensitive detection, *TrAC, Trends Anal. Chem.*, 2015, **67**, 209–216.
8 R. Gui and H. Jin, Recent advances in synthetic methods and applications of photo-luminescent molecularly imprinted polymers, *J. Photochem. Photobiol. C*, 2019, **41**, 100315.
9 F. Li, J. Gao, Y. Li, X. He, L. Chen and Y. Zhang, Selective and sensitive determination of celastrol in traditional Chinese medicine based on molecularly imprinted polymers modified Mn-doped ZnS quantum dots optosensing materials, *Colloids Surf., B*, 2020, **190**, 110929.
10 J. Yao, C. Huang, C. Liu and M. Yang, Upconversion luminescence nanomaterials: a versatile platform for imaging, sensing, and therapy, *Talanta*, 2020, **208**, 120157.
11 J. F. C. Loo, Y. H. Chien, F. Yin, S. K. Kong, H. P. Ho and K. T. Yong, Upconversion and downconversion nanoparticles for biophotonics and nanomedicine, *Coord. Chem. Rev.*, 2019, **400**, 213042.
12 S. Diao, G. Hong, A. L. Antaris, J. L. Blackburn, K. Cheng and H. Dai, Biological imaging without autofluorescence in the second near-infrared region, *Nano Res.*, 2015, **8**, 3027–3034.
13 Q. Yu, C. He, Q. Li, Y. Zhou, N. Duan and S. Wu, Fluorometric determination of acetamiprid using molecularly imprinted upconversion nanoparticles, *Mikrochim. Acta*, 2020, **187**, 222.
14 Y. Tang, H. Liu, J. Gao, X. Liu, X. Gao, X. Lu, G. Fang, J. Wang and J. Li, Upconversion particle@$Fe_3O_4$@molecularly imprinted polymer with controllable shell thickness as high-performance fluorescent probe for sensing quinolones, *Talanta*, 2018, **181**, 95–103.
15 J. M. Liu, F. Z. Cao, G. Z. Fang and S. Wang, Upconversion nanophosphor-involved molecularly imprinted fluorescent polymers for sensitive and specific Recognition of sterigmatocystin, *Polymers*, 2017, **9**, 299.
16 X. Liu, J. Ren, L. Su, X. Gao, Y. Tang, T. Ma, L. Zhu and J. Li, Novel hybrid probe based on double recognition of aptamer-molecularly imprinted polymer grafted on upconversion nanoparticles for enrofloxacin sensing, *Biosens. Bioelectron.*, 2017, **87**, 203–208.
17 T. Guo, Q. Deng, G. Fang, D. Gu, Y. Yang and S. Wang, Upconversion fluorescence metal-organic frameworks thermo-sensitive imprinted polymer for enrichment and sensing protein, *Biosens. Bioelectron.*, 2016, **79**, 341–346.
18 H. W. Chien, C. H. Wu, C. H. Yang and T. L. Wang, Multiple doping effect of $LiYF_4$:$Yb^{3+}$/$Er^{3+}$/$Ho^{3+}$/$Tm^{3+}$@$LiYF_4$:$Yb^{3+}$ core/shell nanoparticles and its application in $Hg^{2+}$ sensing detection, *J. Alloys Compd.*, 2019, **806**, 272–282.
19 H. W. Chien, C. H. Yang, M. T. Tsai and T. L. Wang, Photoswitchable spiropyran-capped hybrid nanoparticles based on UV-emissive and dual-emissive upconverting nanocrystals for bioimaging, *J. Photochem. Photobiol., A*, 2020, **392**, 112303.
20 Y. C. Chung, C. H. Yang, R. H. Lee and T. L. Wang, Dual stimuli-responsive block copolymers for controlled release triggered by upconversion luminescence or temperature variation, *ACS Omega*, 2019, **4**, 3322–3328.
21 H. F. EL-Sharif, H. Yapati, S. Kalluru and S. M. Reddy, Highly selective BSA imprinted polyacrylamide hydrogels facilitated by a metal-coding MIP approach, *Acta Biomater.*, 2015, **28**, 121–127.
22 G. Z. Kyzas, N. K. Lazaridis and D. N. Bikiaris, Optimization of chitosan and β-cyclodextrin molecularly imprinted polymer synthesis for dye adsorption, *Carbohydr. Polym.*, 2013, **91**, 198–208.
23 S. Wen, J. Zhou, P. J. Schuck, Y. D. Suh, T. W. Schmidt and D. Jin, Future and challenges for hybrid upconversion nanosystems, *Nat. Photonics*, 2019, **13**, 828–838.
24 G. Tessitore, G. A. Mandl, M. G. Brik, W. Park and J. A. Capobianco, Recent insights into upconverting nanoparticles: spectroscopy, modeling, and routes to improved luminescence, *Nanoscale*, 2019, **11**, 12015–12029.
25 Y. Fang, L. Liu and F. Zhang, Exploiting lanthanide-doped upconversion nanoparticles with core/shell structures, *Nano Today*, 2019, **25**, 68–84.
26 L. Shi, J. Hu, X. Wu, S. Zhan, S. Hu, Z. Tang, M. Chen and Y. Liu, Upconversion core/shell nanoparticles with lowered surface quenching for fluorescence detection of $Hg^{2+}$ ions, *Dalton Trans.*, 2018, **47**, 16445–16452.
27 Q. Xiao, Y. Ji, Z. Xiao, Y. Zhang, H. Lin and Q. Wang, Novel multifunctional $NaYF_4$:$Er^{3+}$,$Yb^{3+}$/PEGDA hybrid microspheres: NIR-light-activated photopolymerization and drug delivery, *Chem. Commun.*, 2013, **49**, 1527–1529.
28 K. E. Sapsford, L. Berti and I. L. Medintz, Materials for fluorescence resonance energy transfer analysis: beyond traditional donor–acceptor combinations, *Angew. Chem., Int. Ed. Engl.*, 2006, **45**, 4562–4589.
29 A. Bagheri, H. Arandiyan, C. Boyer and M. Lim, Lanthanide-doped upconversion nanoparticles: emerging

intelligent light-activated drug delivery systems, *Adv. Sci.*, 2016, **3**, 1500437.

30 J. Yu, X. Wang, Q. Kang, J. Li, D. Shen and L. Chen, One-pot synthesis of a quantum dot-based molecular imprinting nanosensor for highly selective and sensitive fluorescence detection of 4-nitrophenol in environmental waters, *Environ. Sci.: Nano*, 2017, **4**, 493–502.

31 H. F. Wang, Y. He, T. R. Ji and X. P. Yan, Surface molecular imprinting on Mn-doped ZnS quantum dots for room-temperature phosphorescence optosensing of pentachlorophenol in water, *Anal. Chem.*, 2009, **81**, 1615–1621.

32 Y. Zhang, D. Zhang and H. Liu, Luminescent molecularly imprinted polymers based on covalent organic frameworks and quantum dots with strong optical response to quinoxaline-2-carboxylicacid, *Polymers*, 2019, **11**, 708.

33 T. Guo, Q. Deng, G. Fang, C. Liu, X. Huang and S. Wang, Molecularly imprinted upconversion nanoparticles for highly selective and sensitive sensing of Cytochrome c, *Biosens. Bioelectron.*, 2015, **74**, 498–503.

34 N. W. Turner, C. W. Jeans, K. R. Brain, C. J. Allender, V. Hlady and D. W. Britt, From 3D to 2D: a review of the molecular imprinting of proteins, *Biotechnol. Prog.*, 2006, **22**, 1474–1489.

35 S. Liu, J. Pan, H. Zhu, G. Pan, F. Qiu, M. Meng, J. Yao and D. Yuan, Graphene oxide based molecularly imprinted polymers with double recognition abilities: the combination of covalent boronic acid and traditional non-covalent monomers, *Chem. Eng. J.*, 2016, **290**, 220–231.

36 F. Tasselli, L. Donato and E. Drioli, Evaluation of molecularly imprinted membranes based on different acrylic copolymers, *J. Membr. Sci.*, 2008, **320**, 167–172.

37 E. Verheyen, J. P. Schillemans, M. Wijk, A. Demeniex, W. E. Hennink and C. F. Nostrum, Challenges for the effective molecular imprinting of proteins, *Biomaterials*, 2011, **32**, 3008–3020.

38 L. Chen, S. Xu and J. Li, Recent advances in molecular imprinting technology: current status, challenges and highlighted applications, *Chem. Soc. Rev.*, 2011, **40**, 2922–2942.

39 D. Refaat, M. G. Aggour, A. A. Farghali, R. Mahajan, J. G. Wiklander, I. A. Nicholls and S. A. Piletsky, Strategies for molecular imprinting and the evolution of MIP nanoparticles as plastic antibodies—synthesis and applications, *Int. J. Mol. Sci.*, 2019, **20**, 6304.

 